Charge transfer and a magnetic crossover in hexagonal $BaRu_{1-x}Mn_xO_3$ perovskites

Congling Yin,[1,2] Guobao Li,[2] Winfried A. Kockelmann,[3] Jianhua Lin,[2] and J. Paul Attfield[1]
[1]*Centre for Science at Extreme Conditions and School of Chemistry, University of Edinburgh, King's Buildings, Mayfield Road, Edinburgh EH9 3JZ, United Kingdom*
[2]*Beijing National Laboratory for Molecular Sciences, State Key Laboratory of Rare Earth Materials Chemistry and Applications, College of Chemistry and Molecular Engineering, Peking University, Beijing 100871, People's Republic of China*
[3]*ISIS Facility, Rutherford Appleton Laboratory, Chilton OX11 0QX, United Kingdom*
(Received 25 May 2009; revised manuscript received 30 July 2009; published 25 September 2009)

Charge transfer and cation order degrees of freedom and magnetism have been investigated in hexagonal, 9*R*-type, $BaRu_{1-x}Mn_xO_3$ solid solutions for $0 \leq x \leq 0.9$. The cell parameters and volume follow a "charge transfer Vegard's law," with two linear regions that meet at $x=0.5$ evidencing a significant $Mn^{4+}+Ru^{4+} \rightarrow Mn^{3+}+Ru^{5+}$ charge transfer. Cation order anomalies at $x=1/3$ and 2/3 evidence some Mn/Ru clustering within trimer units. The two charge regimes give rise to distinctive magnetic behaviors. Spin freezing near 25 K is observed for samples with $x<0.4$, but above $x=0.5$ a Néel transition increases from 125 to 270 K at $x=0.9$. Neutron diffraction reveals an antiferromagnetic structure with a $(00\frac{1}{2})$ propagation vector and two-dimensional critical behavior for the $x=0.8$ material.

DOI: 10.1103/PhysRevB.80.094420 PACS number(s): 75.25.+z, 75.47.Lx, 61.66.Fn

I. INTRODUCTION

The electronic properties of transition-metal oxides are a continuing research theme due to the variety of ground states and their potential applications.[1,2] Ruthenium and manganese oxides provide several important perovskite-related electronic materials showing active spin, orbital, or charge degrees of freedom. Sr_2RuO_4 is spin-triplet *p*-wave superconductor below 1 K,[3,4] while $SrRuO_3$ is an itinerant electron ferromagnet.[5,6] Manganese oxide perovskites (manganites) have been extensively studied due to the observation of colossal magnetoresistances, charge order, and electronic phase segregation.[7–10]

Mn and Ru can be substituted for each other in these types of oxide and several series have been investigated such as $CaMn_{1-x}Ru_xO_3$,[11] $SrMn_{1-x}Ru_xO_3$,[12,13] and $Ln_yA_{1-y}Mn_{1-x}Ru_xO_3$ (Ln=lanthanide; *A*=Ca, Sr).[14–17] Ru doping is found to induce ferromagnetism and metallicity and suppresses the charge ordered state of manganites.[13,18] To gain more insight into the interplay between Mn and Ru, we have explored the hexagonal $BaRu_{1-x}Mn_xO_3$ series in which further degrees of freedom such as stacking polytypism and Ru/Mn cation order and charge transfer over multiple sites are available.

$BaRuO_3$ is reported to crystallize in five perovskite-related structures: 3*C*, 4*H*, 6*H*, 9*R*, and 10*H* (this notation shows the number of close-packed layers in the repeat sequence and the lattice symmetry as *C*, *H*, *R*=cubic, hexagonal, rhombohedral),[19–23] and 9*R* is the stable phase under ambient pressure. Stoichiometric $BaMnO_3$ is reported to crystallize in the 2*H* or 15*R* structure depending on the synthesis conditions,[24,25] but a 9*R* structure is found in $Ba_{0.875}Sr_{0.125}MnO_3$.[24] A series of polytypes ($2H \rightarrow 15R \rightarrow 8H \rightarrow 6H \rightarrow 10H \rightarrow 4H$) is found in reduced $BaMnO_{3-y}$ as the oxygen vacancy concentration *y* increases. Previous studies of $BaRu_{1-x}Mn_xO_3$ materials reported a 9*R* structure for $x=0$, 1/3, 1/2, 2/3, but the physical properties were not explored systematically.[22,26–28] In this paper, we report the variation of structural, magnetic, and transport properties across the $BaRu_{1-x}Mn_xO_3$ series.

II. SAMPLE PREPARATION

Polycrystalline $BaRu_{1-x}Mn_xO_3$ samples with compositions shown in Table I were synthesized from stoichiometric $BaCO_3$ (99.9%), $MnCO_3$ (99.9%), and RuO_2 (99.9%). The starting materials were mixed in an agate mortar and pestle and heated in an alumina crucible at 1000 °C for 10 h. The samples were reground, pressed into pellets (under 10 ton/cm^2), heated at 1300 °C for 40 h with several intermediate regrinding and repressing steps, and finally slow-cooled to room temperature.

Single phase 9*R*-type $BaRu_{1-x}Mn_xO_3$ solid solutions were obtained for $0 \leq x \leq 0.9$. Secondary phases are observed above this composition limit, as shown for the $x=0.92$ sample in Fig. 1. Oxygen deficiencies were determined from the weight gains after annealing at 500 °C under flowing oxygen. The samples are essentially oxygen stoichiometric ($y \leq 0.01$ in $BaRu_{1-x}Mn_xO_{3-y}$) at low *x*, but show a slight deficiency up to $y=0.04$ at high *x* values (see Table I). These deficiencies do not significantly affect the measured properties and are neglected in the following discussion.

III. X-RAY DIFFRACTION STUDIES

Powder x-ray diffraction was performed on a Bruker AXS D8 diffractometer with germanium monochromatized Cu $K_{\alpha 1}$ radiation. Data were collected with a PSD detector in continuous scanning mode over 15 h with a 2θ step size of 0.014°. The general structure analysis system (GSAS) package[29] was used to fit a 9*R*-type model [Fig. 2 inset, space group $R\bar{3}m$] to the x-ray diffraction profiles. In addition to the variable lattice parameters and atomic coordinates, the Ru/Mn ratios at the independent *M*1 and *M*2 cation sites were refined subject to the initial stoichiometry. Good fits were obtained for all of the refinements with R_{wp}

TABLE I. Structural parameters for $BaRu_{1-x}Mn_xO_{3-y}$ from fits to room-temperature x-ray diffraction profiles, showing lattice parameters: atomic coordinates, isotropic temperature (U) factors for the cation sites (oxygen atom values were fixed to be 0.025 Å^2), and Mn-site occupancies for M=Mn/Ru sites; the cation order parameter mean δ, M-O and M-M distances, and the oxygen deficiency y measured by thermogravimetry. The structure has space group $R\bar{3}m$. Sites: Ba1: 3a (0 0 0); Ba2: 6c(0 0 z_1); $M1$: 3b (0 0 0.5); $M2$: 6c (0 0 z_2); O1: 18h (x $-x$ z_3); O2: 9e (0.5 0 0).

x	0	0.1	0.2	0.33	0.4	0.5	0.6	0.67	0.75	0.8	0.9
a (Å)	5.7506(1)	5.7431(1)	5.7349(1)	5.7255(1)	5.7203(1)	5.7141(1)	5.7038(1)	5.6989(1)	5.6912(1)	5.6876(1)	5.6773(2)
c (Å)	21.6011(2)	21.5536(3)	21.5011(3)	21.4314(3)	21.3895(3)	21.3287(3)	21.2497(3)	21.1997(3)	21.1331(3)	21.0995(3)	21.0133(7)
V (Å^3)	618.62(2)	615.66(2)	612.41(2)	608.42(2)	606.13(2)	603.11(2)	598.70(2)	596.27(2)	592.78(2)	591.10(2)	586.56(4)
Ba1: U (Å^2)	0.0107(4)	0.0128(5)	0.0117(5)	0.0133(5)	0.0081(5)	0.0132(5)	0.0110(5)	0.0136(5)	0.0107(5)	0.0070(6)	0.0044(10)
Ba2: z_1	0.2175(1)	0.2177(1)	0.2181(1)	0.2185(1)	0.2185(1)	0.2186(1)	0.2187(1)	0.2185(1)	0.2187(1)	0.2192(1)	0.2190(1)
Ba2: U (Å^2)	0.0105(3)	0.0120(4)	0.0110(3)	0.0110(3)	0.0074(4)	0.0097(4)	0.0090(4)	0.0125(4)	0.0107(4)	0.0086(5)	0.0118(9)
$M1$: Occ(Mn)	0	0.137(6)	0.256(7)	0.402(6)	0.513(7)	0.629(6)	0.740(6)	0.816(6)	0.895(6)	0.938(7)	0.990(11)
$M1$: U (Å^2)	0.0114(4)	0.0120(6)	0.0116(7)	0.0137(7)	0.0087(9)	0.0108(8)	0.0074(8)	0.0111(9)	0.0070(10)	0.0078(11)	0.0032(19)
$M2$: z_2	0.3835(1)	0.3837(1)	0.3835(1)	0.3833(1)	0.3834(1)	0.3835(1)	0.3833(1)	0.3832(1)	0.3827(1)	0.3830(1)	0.3815(2)
$M2$: Occ(Mn)	0	0.082(3)	0.172(3)	0.299(3)	0.343(4)	0.435(3)	0.530(3)	0.592(3)	0.678(3)	0.731(4)	0.855(6)
$M2$: U (Å^2)	0.0087(4)	0.0117(4)	0.0112(4)	0.0133(4)	0.0103(5)	0.0142(5)	0.0123(5)	0.0162(6)	0.0132(6)	0.0142(7)	0.0076(13)
O1: x_1	0.1623(4)	0.1609(4)	0.1627(4)	0.1601(4)	0.1587(5)	0.1571(5)	0.1570(5)	0.1566(5)	0.1558(5)	0.1562(6)	0.1560(10)
O1: z_3	0.5582(2)	0.5575(2)	0.5575(2)	0.5576(2)	0.5579(2)	0.5574(2)	0.5575(2)	0.5569(2)	0.5573(2)	0.5574(2)	0.5577(4)
δ	0	0.037(6)	0.056(7)	0.072(6)	0.113(7)	0.129(6)	0.140(6)	0.146(6)	0.145(6)	0.138(7)	0.090(11)
$d_{M1\text{-}O}$ (Å)	2.047(4)	2.025(4)	2.034(4)	2.010(4)	2.002(5)	1.979(4)	1.975(4)	1.961(5)	1.956(5)	1.958(6)	1.955(10)
$d_{M2\text{-}O}$ (Å)	2.016(3)	2.012(3)	2.016(3)	2.000(3)	1.990(3)	1.985(3)	1.978(3)	1.978(3)	1.970(3)	1.968(3)	1.961(6)
$d_{M1\text{-}M2}$ (Å)	2.516(1)	2.506(1)	2.505(2)	2.500(2)	2.495(2)	2.485(2)	2.480(2)	2.477(2)	2.479(2)	2.469(3)	2.491(4)
y	0.011	0.009	0.011	0.014	0.012	0.012	0.024	0.019	0.045	0.041	0.038

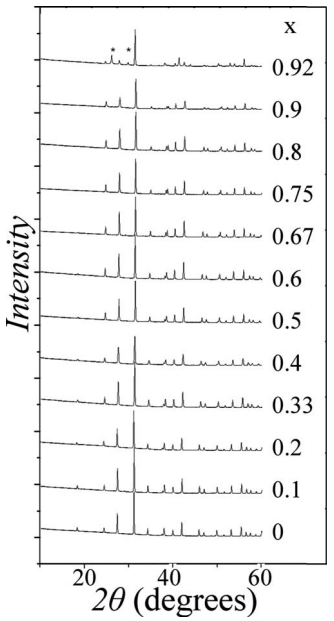

FIG. 1. X-ray diffraction patterns of $BaRu_{1-x}Mn_xO_3$ showing a single 9*R*-type phase for $0 \leq x \leq 0.9$ and secondary phases (marked with an asterisk) for $x=0.92$.

(weighted-profile residual) factors of 2.0%–3.0% and χ^2 (goodness-of-fit) values in the range 1.6–3.0. A typical refinement plot ($x=0.75$) is shown in Fig. 2 and the refined crystallographic parameters and selected bond lengths are shown for all samples in Table I.

No gross chemical or structural discontinuities are evident in the $0 \leq x \leq 0.9$ x-ray data (Fig. 1) and the hexagonal lattice parameters and volume decrease with x as expected given that Mn^{4+} is smaller than Ru^{4+}.[30] However, a notable feature is that these parameters follow two linear regimes that cross over at $x=0.5$, as shown in Fig. 3. This could signify an intermediate structure such as a Mn/Ru ordered arrangement, but this is not supported by the variation of the cation order parameter δ below and is inconsistent with the 1:2 ratio of $M1$:$M2$ sites. A monotonic lattice-parameter variation is expected if Mn^{4+} continuously replaces Ru^{4+} without variation of the charge states, but the discontinuity at $x=0.5$ evidences a substantial intermetallic charge transfer, which may be represented as $Mn^{4+}+Ru^{4+} \rightarrow Mn^{3+}+Ru^{5+}$.

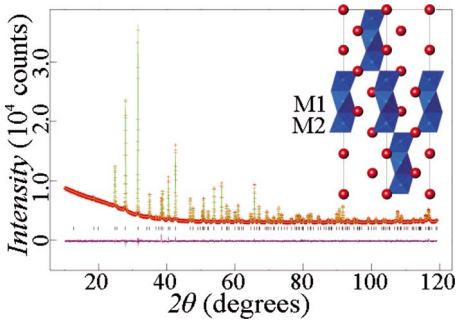

FIG. 2. (Color online) Observed, calculated, and difference x-ray diffraction profile plots for $BaRu_{0.25}Mn_{0.75}O_3$. Inset shows the 9*R*-type structure with Ba as large spheres and the octahedral coordinations by oxygen around the two M=Ru/Mn sites.

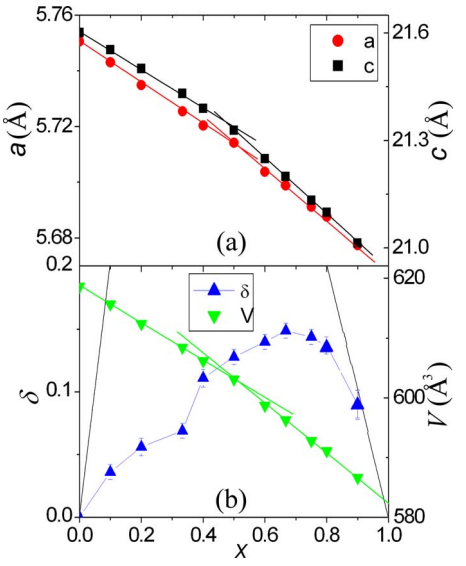

FIG. 3. (Color online) (a) Hexagonal lattice parameters and (b) cation order parameter δ and cell volume variations with x for the 9*R*-$BaRu_{1-x}Mn_xO_3$ solid solutions. The two lattice parameter and volume regimes resulting from charge transfer are fitted by straight lines. The theoretical upper limits for δ are also shown in (b).

If complete transfer occurred in the $BaRu_{1-x}Mn_xO_3$ system, then the charge distributions would be $BaRu^{4+}_{1-2x}Ru^{5+}_xMn^{3+}_xO_3$ for $0 \leq x \leq 0.5$ and $BaRu^{5+}_{1-x}Mn^{3+}_{1-x}Mn^{4+}_{2x-1}O_3$ for $0.5 \leq x \leq 0.9$. The lattice expansion due to complete charge transfer in the solid solutions may be estimated from the sum of six coordinate ionic radii for

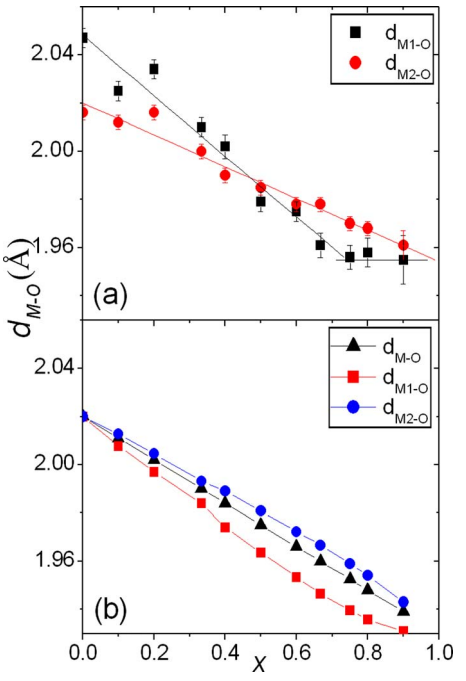

FIG. 4. (Color online) Variations of the mean M-O distances for the two cation sites in the 9*R*-$BaRu_{1-x}Mn_xO_3$ structure with x. (a) Experimental results; (b) calculated distances based on ionic radii and the observed cation order, also showing the expected average M-O distance.

Mn^{3+}(0.645 Å)+Ru^{5+}(0.565 Å), total 1.21 Å, which is slightly greater than that for Mn^{4+}(0.530 Å)+Ru^{4+}(0.620 Å), total 1.15 Å.[30] This difference is 0.06 Å whereas the observed difference is estimated as $2[V_{obs}(0.5)^{1/3}-V_{44}(0.5)^{1/3}] \approx 0.02$ Å, where $V_{obs}(0.5)$ is the observed volume per formula unit for the $x=0.5$ sample and $V_{44}(0.5)$ is the value for hypothetical $BaRu^{4+}_{0.5}Mn^{4+}_{0.5}O_3$ estimated by linear interpolation between the volumes for $x=0$ and $x=1$ (obtained by extrapolation of the $x=0.5-0.9$ behavior) in Fig. 3(b). Hence, the lattice-parameter variation demonstrates a partial charge transfer between Mn and Ru of approximately 1/3 of the theoretical maximum. Future x-ray spectroscopy or Ru Mossbauer measurements may be useful to verify and further study the charge transfer.

The 9*R* hexagonal perovskite structure contains two inequivalent transition-metal ion sites that form trimers of face-sharing octahedra, corner linked into layers, as shown in Fig. 2. The high Mn/Ru x-ray scattering contrast enables the occupancies of the two sites to be refined precisely. To quantify the degree of cation segregation, we define an order parameter as δ=(occupancy of Mn at the *M*1 site)$-x$. This corresponds to an occupancy formula $Ba(Ru1_{1-x-\delta}Mn1_{x+\delta})_{1/3}(Ru2_{1-x+\delta/2}Mn2_{x-\delta/2})_{2/3}O_3$, where Ru1 corresponds to Ru at the *M*1 site, etc. $\delta=0$ would correspond to statistical site occupancies, but the positive values of δ found for all $0<x\leq 0.9$ [Fig. 3(b)] reveal a preferential occupancy of Mn for the *M*1 sites and Ru for *M*2 sites.

For complete cation segregation, two linear δ-x regions meeting at a maximum of $\delta=2/3$ for $x=1/3$ (i.e., $BaMn1_{1/3}Ru2_{2/3}O_3$) would be observed. The observed trend in Fig. 3(b) is more complex. δ increases with x up to $x=2/3$, showing that the site preference increases as the lattice contracts [Fig. 3(a)]. At higher x, δ decreases toward the theoretical limit and a full Mn occupancy of the *M*1 site is observed at $x=0.9$. The features observed at $x=1/3$ and 2/3 evidence cluster formation within the *M*2*M*1*M*2 trimer units. The observation of maximal cation ordering at $x=2/3$ indicates that Mn2Mn1Ru2 clusters are stabilized, whereas the pronounced dip in δ at $x=0.33$ reveals a local stabilization of Mn2Ru1Ru2 clusters relative to the general tendency to form Ru2Mn1Ru2 units. The stabilization of the former trimers may reflect local Ru-Ru bonding, as evidenced in the *M*-O bond distances below.

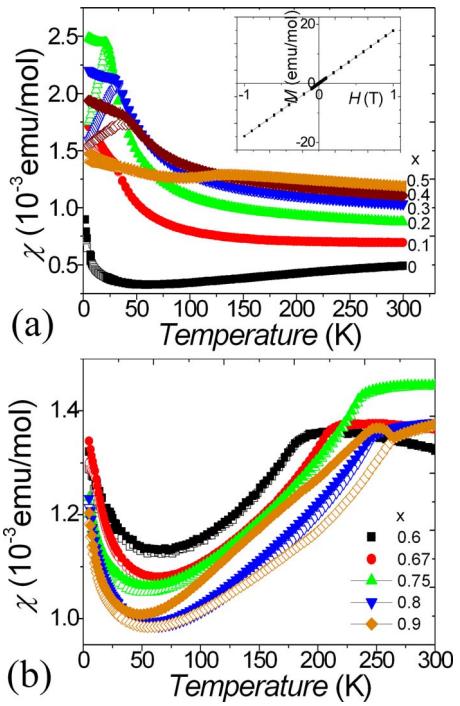

FIG. 5. (Color online) Magnetic susceptibilities for $BaRu_{1-x}Mn_xO_3$: (a) $x=0-0.5$; (b) $x=0.6-0.9$; with filled/open symbols showing field-cooled /zero-field-cooled data. Inset to (a) shows the magnetization-field loop for the $x=0.2$ sample at 5 K.

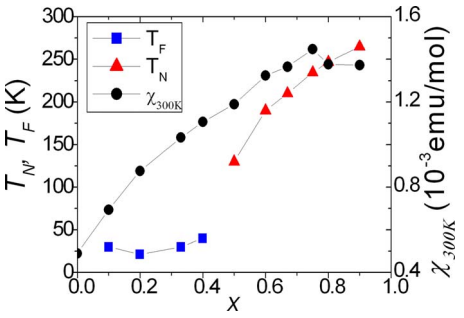

FIG. 6. (Color online) Variations of the spin freezing and Néel temperatures and the 300 K magnetic susceptibility with x for $BaRu_{1-x}Mn_xO_3$.

The variations of the *M*-O distances are shown in Fig. 4 together with calculated distances based on ionic radii and the observed cation order. The presence of active charge transfer and cation order degrees of freedom precludes a detailed analysis of the average distances, as the distribution of charge states for Mn and Ru between the two sites is unknown. However, cation charge and ordering effects cannot explain the disparity between the *M*1-O and *M*2-O distances in the $0\leq x<0.5$ region, as this includes $BaRuO_3$ ($x=0$) for which no cation order or charge transfer is possible. This difference most probably originates in the formation of Ru-Ru bonds across the shared octahedral faces through direct 4*d* orbital overlap, as the Ru-Ru distances are relatively short (2.52 Å). This expands the coordination sphere of the central *M*1 site more than that of the terminal *M*2 sites within the trimers (if the metal-metal bonds are included then

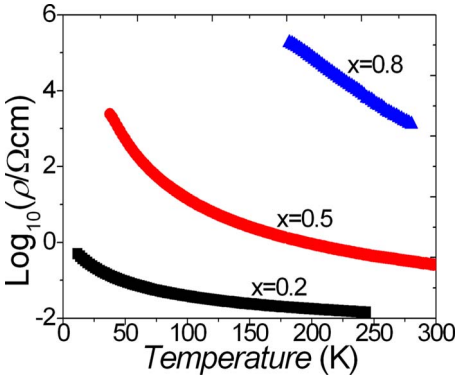

FIG. 7. (Color online) Log_{10}(resistivity) vs temperature data for three $BaRu_{1-x}Mn_xO_3$ samples.

TABLE II. Parameters from fits of the equation $\chi = A + C/(T-\theta)$ to the zero-field-cooled susceptibilities [Fig. 5(a)] of the $BaRu_{1-x}Mn_xO_3$ samples with $x=0.1-0.4$ in the temperature range 50–300 K above the spin-freezing transition. The effective paramagnetic moments per formula unit, μ_{eff}, derived from the Curie constants C are also shown.

x	0.1	0.2	0.33	0.4
A (emu mol^{-1})	$6.42(2)\times10^{-4}$	$7.74(1)\times10^{-4}$	$9.15(2)\times10^{-4}$	$9.83(3)\times10^{-4}$
C (emu K mol^{-1})	0.0121(3)	0.0295(2)	0.0364(4)	0.0415(9)
μ_{eff} (μ_B)	0.31	0.49	0.54	0.58
θ (K)	21(1)	9.9(3)	4.8(5)	−10(1)

the formal $M1$ and $M2$ coordination numbers become 8 and 7, respectively) and so the six-coordinate ionic radius of Ru^{4+} is an underestimate of the true size. This Ru-Ru bonding effect diminishes with increasing Mn substitution. The $M1$-O and $M2$-O distances cross over near $x=0.5$ and at higher x, the average $M2$-O distance is shorter than that for $M1$-O and becomes constant for $x=0.75-0.9$ samples. The observed distances in this region are in reasonable agreement with the predicted values in Fig. 4(b) based on the different cation occupancies of the two sites.

IV. MAGNETIZATION AND RESISTIVITY MEASUREMENTS

Magnetization measurements were recorded in a 1000 Oe field while warming the sample from 5 to 300 K, following zero-field cooling (ZFC), and field cooling (FC), using a Quantum Design superconducting quantum interference device (SQUID) magnetometer. The magnetizations for all of the $BaRu_{1-x}Mn_xO_3$ samples are shown in Fig. 5. Distinctive regimes are observed above and below $x=0.5$, demonstrating an influence of the intermetallic charge transfer.

$BaRuO_3$ has a Pauli-type susceptibility that increases slightly with temperature, as reported previously,[31] and a small Curie tail at low temperatures that probably arises from paramagnetic impurities. Mn doping up to $x=0.4$ increases the overall susceptibility (300 K values are shown in Fig. 6) and introduces a magnetic transition at approximately 25 K, below which the FC and ZFC magnetizations diverge. The magnetization-field loop for the $x=0.2$ sample at 5 K [Fig. 5(a) inset] does not reveal significant hysteresis, showing that the 25 K feature is most likely a spin-freezing transition. Above the freezing temperature T_F, the susceptibilities of the $x=0.1-0.4$ samples are fitted well by a sum of temperature-independent Pauli and Curie-Weiss terms and the derived parameters are shown in Table II. Both the Pauli susceptibility (A) and the Curie constant (C) increase with Mn doping x. The paramagnetic moments derived from the latter term are much smaller than expected for localized Mn spins, with or without Ru/Mn charge transfer, e.g., for $x=0.1$, the observed $\mu_{eff}=0.31\mu_B$ is equivalent to 0.006 localized Mn^{4+} spins per $BaRu_{0.9}Mn_{0.1}O_3$ formula unit. This shows that charge transfer results in some electron delocalization between $Ru^{4+/5+}$ and $Mn^{3+/4+}$ states, enhancing the Pauli susceptibility and diminishing the Curie term, although the substitutional disorder appears to suppress full electron itinerancy as evidenced by the resistivity measurements below. This is in contrast to the $6H$-type $Ba_{0.7}Sr_{0.3}Ru_{1-x}Mn_xO_3$ materials where full paramagnetic Mn moments are observed at low dopings.[32] The small fraction of localized spins in the low-doped $BaRu_{1-x}Mn_xO_3$ series freezes at $T_F \approx 25$ K and no x dependence of T_F is apparent (Fig. 6). The Weiss temperature changes from positive to negative values as x increases, consistent with the growth of antiferromagnetic correlations between localized spins, as observed at $x>0.5$.

Samples with $0.5 \leq x \leq 0.9$ (Fig. 5) show a different (Néel) magnetic transition to the first half of the series and the Néel temperature T_N increases strongly with x, from 125 to 270 K. The 300 K susceptibility changes little in this region (Fig. 6) and the range of susceptibility data above T_N is too small to allow meaningful analysis of the paramagnetic susceptibilities. No FC-ZFC magnetization divergence is seen at the transitions of the $x=0.5-0.75$ samples showing that the spin-ordered state is antiferromagnetic. However, a divergence is evident for $x=0.8$ and 0.9 indicating that some spin canting (weak ferromagnetism) occurs. The antiferromagnetic insulator behavior is consistent with the charge distribution for this regime as the mixture of mainly $S=3/2$ Ru^{5+} and Mn^{4+}, and $S=2$ Mn^{3+} ions leads to predominantly antiferromagnetic interactions, although local-orbital ordering of Mn^{3+} could create some ferromagnetic couplings causing frustration. The presence of residual paramagnetic spins is evident by the low-temperature Curie tails in the $x=0.6-0.9$ susceptibilities.

Resistivities of sintered polycrystalline bars (approximate dimensions $3\times3\times10$ mm^3) of three $BaRu_{1-x}Mn_xO_3$ samples were recorded using a standard four-probe dc technique on a Quantum Design physical property measurement system and are shown in Fig. 7. $BaRuO_3$ is a metallic oxide[20] and the $\sim10^{-2}$ Ω cm value of the high-temperature resistivity for the $x=0.2$ sample is consistent with metallic behavior. However, disorder or grain-boundary scattering introduces a semiconductor-type bulk-temperature dependence that does not follow an Arrhenius or other simple variations. No resistive transition is evident at the 25 K spin-freezing transition for the $x=0.2$ sample, confirming that only a small fraction of localized spins are involved. The electronic behavior of $BaRu_{1-x}Mn_xO_3$ evolves from metal-like to insulating with an increase of 6 orders of magnitude in the resistivity between $x=0.2$ and 0.8.

V. NEUTRON DIFFRACTION STUDIES

Low-temperature neutron diffraction was used to investigate magnetic order and any lattice distortions in samples

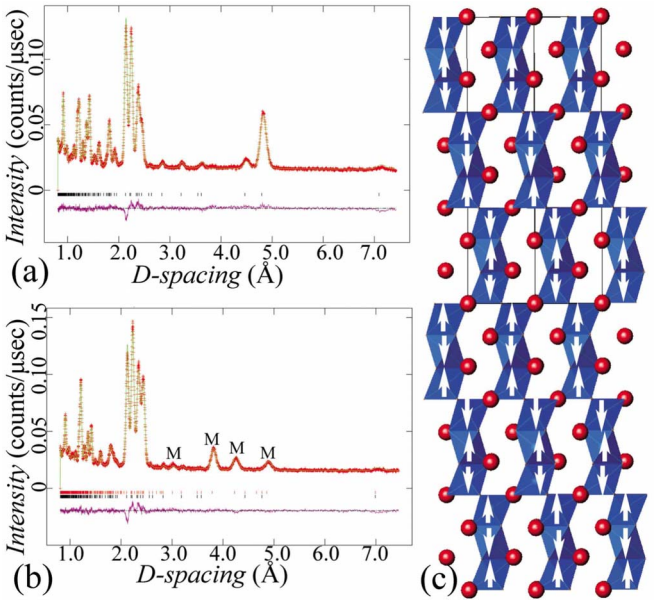

FIG. 8. (Color online) Fits to the 5 K neutron diffraction profiles of (a) $BaRu_{0.6}Mn_{0.4}O_3$, containing only nuclear peaks, and (b) $BaRu_{0.2}Mn_{0.8}O_3$, in which the magnetic peak (M) intensities are calculated from the antiferromagnetically ordered superstructure shown in (c).

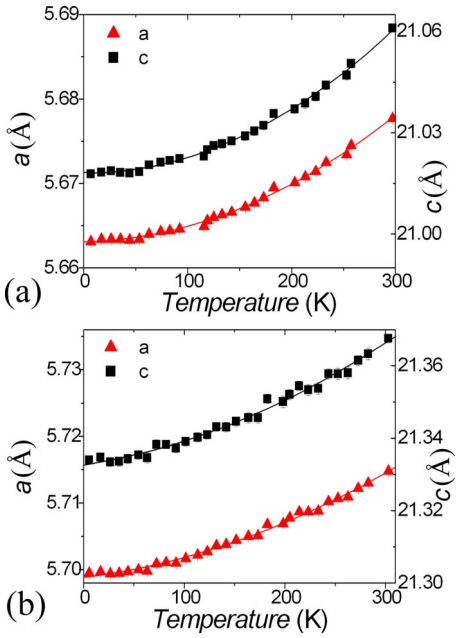

FIG. 9. (Color online) Lattice parameter variations with temperature for (a) $BaRu_{0.2}Mn_{0.8}O_3$ and (b) $BaRu_{0.6}Mn_{0.4}O_3$.

from the above two distinctive magnetic regimes ($x=0.4$ and 0.8). Data were collected on the time-of-flight GEM diffractometer at the ISIS spallation neutron source between 5 and 300 K.

No additional Bragg scattering was observed in the neutron diffraction patterns of $BaRu_{0.6}Mn_{0.4}O_3$ down to 5 K, showing that long-range spin order does not occur below the 25 K freezing transition, but additional magnetic peaks are observed below the 260 K Néel transition for $BaRu_{0.2}Mn_{0.8}O_3$ (Fig. 8). These are indexed by the $(00\frac{1}{2})$ propagation vector and the intensities are fitted by the model shown in Fig. 8(c) using standard magnetic scattering factors.[29] The spins are parallel to the c axis and are antiferromagnetically coupled to their neighbors within and between trimer units in all directions. The saturated moment of $2.18\mu_B$ at 5 K is reduced from the ideal value of $2.93\mu_B$ (from the charge distribution $2/3(BaRu^{4+}_{0.2}Mn^{4+}_{0.8}O_3)$ $+1/3(BaRu^{5+}_{0.2}Mn^{3+}_{0.2}Mn^{4+}_{0.6}O_3)$, based on the x-ray diffraction estimate of the charge transfer and assuming spin-only saturated moments for low-spin Ru^{4+} and high-spin Mn^{3+}) due to typical zero-point and covalence effects.[33] Disorder may also contribute to the moment reduction, but no substantial decrease arising from frustration is evident.

The cell parameters and volumes for the two $BaRu_{1-x}Mn_xO_3$ samples show normal thermal-expansion behavior (Figs. 9 and 10) without magnetostrictive anomalies at the spin-freezing or ordering transitions or any other lattice distortions. The refined crystal structures at 5 K in Table III are very similar to the room-temperature x-ray structures. The thermal evolution of the refined magnetic moment for $BaRu_{0.2}Mn_{0.8}O_3$ is shown in Fig. 10(a). The temperature variation of the moment was fitted as $\mu=\mu_0(1-T/T_N)^{\beta}$, giving fitted values of $T_N=260.0(5)$ K and $\beta=0.257(3)$. The critical exponent is close to the calculated value of 0.25 for a two-dimensional Heisenberg magnet,[34] in keeping with the broad susceptibility peak for this sample [Fig. 5(b)]. This two-dimensional magnetic character is also in keeping with the geometries of the M-O-M bridges (Table III) which mediate the superexchange interactions between spins. The strongest antiferromagnetic exchange is obtained for the 180° $M2$-O-$M2$ linkages between trimers, which connect

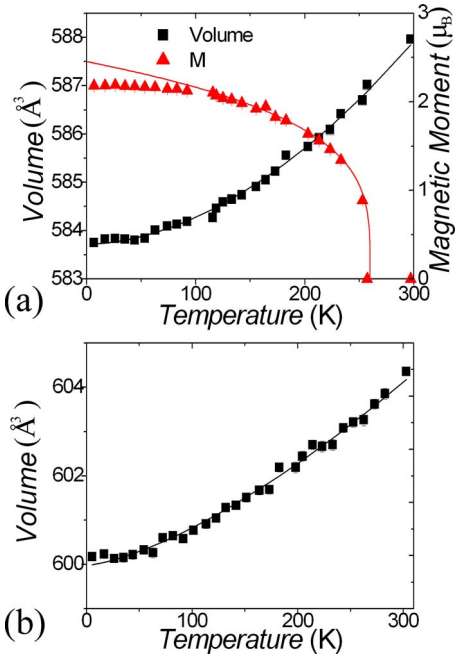

FIG. 10. (Color online) Cell volume variations with temperature for (a) $BaRu_{0.2}Mn_{0.8}O_3$ and (b) $BaRu_{0.6}Mn_{0.4}O_3$. (a) also shows the critical variation of the ordered magnetic moment, fitted in the region $T_N/2<T<T_N$, where $T_N=260$ K.

TABLE III. Refinement results from fitting the 5 K neutron diffraction profiles for the $x=0.4$ and 0.8 samples of $BaRu_{1-x}Mn_xO_3$. The U factors and the magnetic moment for $x=0.8$ were constrained to be the same for $M1$ and $M2$. Mn/Ru site occupancies were fixed at the values shown in Table I.

x	0.4	0.8	x	0.4	0.8
a (Å)	5.6995(3)	5.6631(3)	O1:z_3	0.5579(1)	0.5578(1)
c (Å)	21.3340(10)	21.0178(9)	O1:U (Å^2)	0.0044(1)	0.0041(1)
V/Å^3	600.17(8)	583.75(7)	O2:U (Å^2)	0.0047(1)	0.0037(1)
Ba1:U (Å^2)	0.0017(2)	0.0017(2)	$d_{M1\text{-}O1}$ (Å)	1.9551(4)	1.903(1)
Ba2:z_1	0.2187(1)	0.2192(1)	$d_{M2\text{-}O1}$ (Å)	1.9593(9)	1.960(3)
Ba2:U (Å^2)	0.0010(1)	0.0011(1)	$d_{M2\text{-}O2}$ (Å)	1.9676(7)	1.909(3)
$M1$:U (Å^2)	0.0007(2)	0.0024(3)	$d_{M1\text{-}M2}$ (Å)	2.477(1)	2.517(5)
$M1$:μ_z (μ_B)	0	2.18(1)	$M2$-O1-M2	180.0	180.0
$M2$:z_2	0.3839(1)	0.3803(2)	$M1$-O2-M2	78.50(3)	81.29(11)
O1:x_1	0.1536(1)	0.1494(1)	R_{wp} (%)	3.91	4.65

corrugated layers of spins parallel to the xy plane. These layers are connected through $M1$ spins via weaker interactions within trimers for which the $M1$-O-$M2$ angle is 81°.

VI. CONCLUSIONS

$9R$-type $BaRu_{1-x}Mn_xO_3$ solid solutions can be prepared over the range $0 \leq x \leq 0.9$. Although the structure appears to evolve continuously, detailed structural analysis demonstrates that fractional discontinuities are introduced by active charge transfer and cation order degrees of freedom: at $x=1/2$ by partial $Mn^{4+}+Ru^{4+} \rightarrow Mn^{3+}+Ru^{5+}$ charge transfer and at $x=1/3$ and 2/3 by partial cation order over the Mn/Ru crystallographic sites which are in a 1:2 ratio in the $9R$ structure. The charge transfer creates excess volume that results in a "charge transfer Vegard's law" behavior of the unit-cell parameters, with two linear regions that meet at $x=0.5$ corresponding to solid solutions between $BaRu^{4+}O_3$ and $BaRu^{5+}_{0.5}Mn^{3+}_{0.5}O_3$ and between $BaRu^{5+}_{0.5}Mn^{3+}_{0.5}O_3$ and hypothetical $9R$-$BaMn^{4+}O_3$, in the limit of maximum charge transfer. A similar charge transfer Vegard's law was observed in cubic-type $SrRu_{1-x}Cr_xO_3$ perovskites resulting from the analogous $Cr^{4+}+Ru^{4+} \rightarrow Cr^{3+}+Ru^{5+}$ band overlap.[35] The purely electronic origin of the volume crossover at $x=0.5$ in $9R$-$BaRu_{1-x}Mn_xO_3$ is supported by the absence of an accompanying anomaly in the cation order parameter δ. By contrast, the cation ordering anomalies at $x=1/3$ and 2/3 due to the stabilization of Ru_2Mn or $MnRu_2$ trimers are too slight to give rise to observable lattice-parameter anomalies.

The two charge transfer regions lead to distinctive magnetic behaviors above and below $x=0.5$. Low x materials show substantial electron delocalization with significant Pauli susceptibilities and a small fraction of localized spins that freeze at low temperatures. No long-range magnetic order is evident below T_F by neutron scattering for the investigated $x=0.4$ sample. The $x>0.5$ materials are disordered antiferromagnets where the ordering temperature is suppressed by Ru doping into hypothetical $9R$-$BaMnO_3$ which has a projected T_N of 275 K. Neutron diffraction reveals long-range antiferromagnetic order below 260 K for the $x=0.8$ sample. This shows two-dimensional Heisenberg magnet behavior due to strong superexchange within corrugated layers of $M2$ spins, with weaker interlayer interactions mediated through the $M2M1M2$ trimer units.

This study demonstrates that cation order and intermetallic charge transfer may be significant degrees of freedom in mixed Mn/Ru oxides with complex structures, in addition to the usual spin, orbital, and charge degrees for each metal. Further research into such materials is warranted as the $4d$ band of Ru is well-matched to the $3d$ bands of first row transition metals in oxides and the resulting charge transfer often stabilizes interesting electronic ground states. Other examples include superconductivity in $RuSr_2GdCu_2O_8$,[36,37] metallicity in $CaCu_3Ru_4O_{12}$,[38] and high-temperature antiferromagnetism in $SrRu_{1-x}Cr_xO_3$.[35]

ACKNOWLEDGMENTS

We thank China Scholarship Council for financial support for a visiting project. This work is supported by the National Natural Science Foundation of China (Grant 20771008), EPSRC, and the Leverhulme Trust.

[1] C. N. R. Rao and J. Gopalakrishnan, *New Directions in Solid State Chemistry* 2nd ed. (Cambridge University Press, New York, 1997).

[2] C. N. R. Rao and B. Raveau, *Transition Metal Oxides: Structure, Properties and Synthesis of Ceramic Oxides* 2nd ed. (Wiley-VCH, New York, 1998).

[3] K. Ishida, H. Mukuda, Y. Kitaoka, K. Asayama, Z. Q. Mao, Y. Mori, and Y. Maeno, Nature (London) **396**, 658 (1998).

[4] G. M. Luke, Y. Fudamoto, K. M. Kojima, M. I. Larkin, J. Merrin, B. Nachumi, Y. J. Uemura, Y. Maeno, Z. Q. Mao, Y. Mori,

H. Nakamura, and M. Sigrist, Nature (London) **394**, 558 (1998).
[5] R. J. Bouchard and J. L. Gillson, Mater. Res. Bull. **7**, 873 (1972).
[6] J. M. Longo, P. M. Raccah, and J. B. Goodenough, J. Appl. Phys. **39**, 1327 (1968).
[7] E. Dagotto, T. Hotta, and A. Moreo, Phys. Rep. **344**, 1 (2001).
[8] Y. Tokura, A. Urushibara, Y. Moritomo, T. Arima, A. Asamitsu, G. Kido, and N. Furukawa, J. Phys. Soc. Jpn. **63**, 3931 (1994).
[9] C. R. Serrao, A. Sundaresan, and C. N. R. Rao, J. Phys.: Condens. Matter **19**, 496217 (2007).
[10] P. Murugavel, C. Narayana, A. K. Sood, S. Parashar, A. R. Raju, and C. N. R. Rao, Europhys. Lett. **52**, 461 (2000).
[11] A. Maignan, C. Martin, M. Hervieu, and B. Raveau, Solid State Commun. **117**, 377 (2001).
[12] X. Y. Zhang, Y. Chen, Z. Y. Li, C. Vittoria, and V. G. Harris, J. Phys.: Condens. Matter **19**, 266211 (2007).
[13] G. Cao, S. Chikara, X. N. Lin, E. Elhami, V. Durairaj, and P. Schlottmann, Phys. Rev. B **71**, 035104 (2005).
[14] L. S. Lakshmi, V. Sridharan, D. V. Natarajan, R. Rawat, S. Chandra, V. S. Sastry, and T. S. Radhakrishnan, J. Magn. Magn. Mater. **279**, 41 (2004).
[15] A. Maignan, C. Martin, M. Hervieu, and B. Raveau, J. Appl. Phys. **89**, 500 (2001).
[16] P. V. Vanitha, A. Arulraj, A. R. Raju, and C. N. R. Rao, C. R. Acad. Sci., Ser. IIc: Chim. **2**, 595 (1999).
[17] P. M. Woodward, J. Goldberger, M. W. Stoltzfus, H. W. Eng, R. A. Ricciardo, P. N. Santhosh, P. Karen, and A. R. Moodenbaugh, J. Am. Ceram. Soc. **91**, 1796 (2008).
[18] R. K. Sahu, Z. Hu, M. L. Rao, S. S. Manoharan, T. Schmidt, B. Richter, M. Knupfer, M. Golden, J. Fink, and C. M. Schneider, Phys. Rev. B **66**, 144415 (2002).
[19] J. G. Zhao, L. X. Yang, Y. Yu, F. Y. Li, R. C. Yu, Z. Fang, L. C. Chen, and C. Q. Jin, J. Solid State Chem. **180**, 2816 (2007).
[20] T. Ogawa and H. Sato, J. Alloys Compd. **383**, 313 (2004).
[21] S. T. Hong and A. W. Sleight, J. Solid State Chem. **128**, 251 (1997).
[22] P. C. Donohue, L. Katz, and R. Ward, Inorg. Chem. **4**, 306 (1965).
[23] C. Q. Jin, J. S. Zhou, J. B. Goodenough, Q. Q. Liu, J. G. Zhao, L. X. Yang, Y. Yu, R. C. Yu, T. Katsura, A. Shatskiy, and E. Ito, Proc. Natl. Acad. Sci. U.S.A. **105**, 7115 (2008).
[24] J. J. Adkin and M. A. Hayward, Chem. Mater. **19**, 755 (2007).
[25] T. Negas and R. S. Roth, J. Solid State Chem. **3**, 323 (1971).
[26] S. S. Pillai, S. N. Jammalamadaka, and P. N. Santhosh, IEEE Trans. Magn. **43**, 3076 (2007).
[27] Z. S. Gonen, J. Gopalakrishnan, B. W. Eichhorn, and R., L. Greene, Inorg. Chem. **40**, 4996 (2001).
[28] H. U. Schaller, A. Ehmann, and S. Kemmler-Sack, Mater. Res. Bull. **19**, 517 (1984).
[29] A. C. Larson and R. B. Von Dreele, Los Alamos National Laboratory Report No. LAUR 86-748, 2004 (unpublished).
[30] R. D. Shannon, Acta Crystallogr. **A32**, 751 (1976).
[31] J. T. Rijssenbeek, R. Jin, Y. Zadorozhny, Y. Liu, B. Batlogg, and R. J. Cava, Phys. Rev. B **59**, 4561 (1999).
[32] C. Yin, G. Li, J. Lin, and J. P. Attfield, Chem. Asian J. **4**, 969 (2009).
[33] J. F. Vente, K. V. Kamenev, and D. A. Sokolov, Phys. Rev. B **64**, 214403 (2001).
[34] H. Stanley, *Introduction to Phase Transitions and Critical Phenomena* (OUP, Oxford, 1971).
[35] A. J. Williams, A. Gillies, J. P. Attfield, G. Heymann, H. Huppertz, M. J. Martinez-Lope, and J. A. Alonso, Phys. Rev. B **73**, 104409 (2006).
[36] A. C. Mclaughlin, V. Janowitz, J. A. McAllister, and J. P. Attfield, Chem. Commun. 1331 (2000).
[37] A. C. Mclaughlin, V. Janowitz, J. A. McAllister, and J. P. Attfield, J. Mater. Chem. **11**, 173 (2001).
[38] M. A. Subramanian and A. W. Sleight, Solid State Sci. **4**, 347 (2002).